applied sciences

MDPI

Article

EM-Driven Multi-Objective Optimization of a Generic Monopole Antenna by Means of a Nested Trust-Region Algorithm

Adrian Bekasiewicz [1,*], Slawomir Koziel [1,2], Piotr Plotka [1] and Krzysztof Zwolski [1]

[1] Faculty of Electronics Telecommunications and Informatics, Gdansk University of Technology, Narutowicza 11/12, 80-233 Gdansk, Poland; koziel@ru.is (S.K.); piotr.plotka@pg.edu.pl (P.P.); krzysztof.zwolski@pg.edu.pl (K.Z.)

[2] Department of Engineering, Reykjavik University, Menntavegur 1, 101 Reykjavik, Iceland

* Correspondence: bekasiewicz@ru.is

Featured Application: Determination of trade-offs between conflicting design objectives in order to verify usefulness of the antenna for a range of application scenarios.

Abstract: Antenna structures for modern applications are characterized by complex and unintuitive topologies that are difficult to develop when conventional, experience-driven techniques are of use. In this work, a method for the automatic generation of antenna geometries in a multi-objective setup has been proposed. The approach involves optimization of a generic spline-based radiator with an adjustable number of parameters using a nested, trust region-based algorithm. The latter iteratively increases the dimensionality of the radiator in order to gradually improve its performance. The method has been used to generate a set of nine antenna designs, representing a trade-off between minimization of reflection within 3.1 GHz to 10.6 GHz and a reduction of size. The properties of the optimized designs vary along the Pareto set from −10 dB to −20 dB and from 230 mm^2 to 757 mm^2 for the first and second objectives, respectively. The presented design approach has been validated against a genuine, population-based optimization routine. Furthermore, the smallest Pareto-optimal design has been compared to the antennas from the literature.

Keywords: adjustable dimensionality; EM-driven design; multi-objective optimization; nested optimization; UWB antennas

Citation: Bekasiewicz, A.; Koziel, S.; Plotka, P.; Zwolski, K. EM-Driven Multi-Objective Optimization of a Generic Monopole Antenna by Means of a Nested Trust-Region Algorithm. *Appl. Sci.* **2021**, *11*, 3958. https://doi.org/10.3390/app11093958

Academic Editor: Ernesto Limiti

Received: 31 March 2021
Accepted: 22 April 2021
Published: 27 April 2021

1. Introduction

Ultra-wideband (UWB) antennas belong to the key components of modern location and tracking systems capable of providing centimeter-level accuracy [1–6]. For the mentioned services, the radiators may find application not only to data exchange, but also as energy harvesting devices that provide the necessary power for sensors [7–10]. A variety of application scenarios for tracking and location devices impose a range of potential requirements on antenna performance (in terms of field and electrical properties), as well as its dimensions (small footprint or specific shape) [10–15]. Consequently, a coherent system often comprises a range of antenna solutions.

The development of radiators for UWB applications is widely covered in the available literature [16–24]. Conventional design solutions include a range of planar components, such as monopoles [17,18] or dipoles [19,20] as well as volumetric structures [21,22]. Other antennas implement non-standard features that permit performance enhancement by excluding or including specific frequency bands [18,23] or implementing composite topologies to achieve multiple-input multiple-output capability [24,25]. Although the discussed antennas are characterized by varying dimensions or performance, their geometries stem from the mentioned basic topologies [16–24]. Consequently, enhanced functionality of the

latter is often achieved through the introduction of specific geometry abbreviations (e.g., slots [23], stubs [24], perforations [11], or combinations thereof [16]). The modifications are predominantly introduced as a result of manual or semi-manual development, realized in a trial-and-error manner and oriented toward balancing the complexity and performance or size of the radiator [23,24].

Other approaches to the generation of an antenna structure involve representation of its geometry using a set of characteristic points interconnected by lines or appropriately defined curves [26–30]. Alternatively, the topology can be defined using a binary matrix (often with overlapping components with variable dimensions) [31–33], [34] where zeros and ones correspond to the areas with etched or continuous metallization [32]. Contrary to conventional radiators, antenna topologies described using generic models are predominantly determined using optimization methods [35–39]. Notwithstanding, the applicability of numerical algorithms to the generation of unconventional geometries is often demonstrated based on relatively simple, single-objective problems [28,29]. Furthermore, the optimization of generic models is normally undertaken using population-based routines (e.g., particle swarm optimization, genetic algorithms, or ant colony methods), which require thousands of evaluations to obtain the final solution [31,35,38,40]. To put that into perspective, in [41], the particle swarm algorithm required a total of 248 EM simulations to solve a set of 12 problems represented using only one input parameter. In [42], the same method required over 1400 model evaluations to find an optimal design of frequency selective surface represented using three adjustable variables. Due to the high evaluation cost (being in the order of minutes to hours), the application of conventional, population-based routines for the EM-driven optimization of antennas defined using generic models is impractical from a computational standpoint.

The design of modern antennas is a multi-objective (MO) problem, where a set of performance or geometry requirements is to be simultaneously fulfilled [38,43,44]. Conventional approaches to MO tasks involve conversion of the performance requirements into a single-objective function using aggregation techniques, penalty components, or design constraints [35,39,43]. The design task, formulated in this manner, can be solved using conventional single-objective routines [35,43]. On the other hand, aggregation techniques provide only one solution to the problem per algorithm run, whereas the quality of the result depends on the weights assigned to individual figures of interest [35]. Alternatively, MO optimization can be performed using the genuine MO algorithms [39,43]. The latter ones are especially useful when the designer's priorities are not clearly defined, as they provide a set of solutions representing trade-offs between the requirements. Such cognitive studies are useful from the perspective of gaining a detailed insight into the capabilities of the antenna, with respect to the desired application scenarios or environments [45]. Although multi-objective problems could be solved using population-based metaheuristic methods, their practical applications are limited to rather simple structures due to the prohibitive computational cost [35,37]. Less numerically demanding routines involve the execution of evolutionary algorithms on the approximation models. Due to the curse of dimensionality [46], the usefulness of approximation models and metaheuristics for reliable MO optimization is limited either to low-dimensional structures or narrow search spaces [43,47]. Notwithstanding, the mentioned methods proved to be useful for solving problems characterized by over a dozen design parameters [43]. Alternatively, MO design can be handled using dedicated heuristic approaches oriented toward the sequential generation of Pareto-optimal solutions [43,47]. Nonetheless, neither of the mentioned methods are suitable for handling antenna models characterized by a flexible number of adjustable parameters.

The above considerations indicate that contemporary UWB antennas can be categorized into a few classes [16–24]. The topologies from each group are similar except for features such as slots or stubs that are normally introduced as a result of manual, greedy search-based studies to alter the functionality of the structure. In this regard, representation of the antenna using a generic model might be useful for the automated development of

its topology regarding the imposed performance and geometry requirements. Although "universal" antenna models have been reported in the literature, they lack flexibility in terms of the number of degrees of freedom used for their representation. Consequently, they are either too simple or too complex (parameter-wise) to obtain compromise designs. The application of generic topology (or its derivatives) for a range of application scenarios should reduce the cost of system development, as well as its time to market. Unfortunately, the available MO routines are inadequate for handling models with flexible parameterization due to the lack of mechanisms for the adjustment of problem dimensionality in the course of the optimization process. The motivation of this work is to address the mentioned challenges.

In this paper, a generic EM model of a planar antenna with flexible parameterization is presented. The structure is optimized in a bi-objective setup concerning minimization of in-band reflection within a 3.1 GHz to 10.6 GHz band and size. A set of designs, representing the trade-off between the requirements, is obtained using a novel framework that sequentially generates candidate solutions. The latter are refined in a nested trust region-based optimization loop that enables one to gradually increase the number of parameters. The proposed model and optimization framework are demonstrated through the generation of nine Pareto-optimal designs. Their geometries are represented using 30 to 46 input parameters. The variability of the antenna's in-band performance and size along the Pareto set is from −10.3 dB to −20.5 dB (over 10 dB) and from 230 mm^2 to 757 mm^2 (almost 70 percent), respectively. The presented algorithm has been compared against other population-based metaheuristic routines in terms of optimization cost and the quality of obtained solutions. Numerical validation of the generated designs and comparisons of the smallest obtained UWB structure with the state-of-the-art compact antennas are also provided.

2. Generic UWB Monopole Antenna

Consider a planar monopole antenna, shown in Figure 1. The structure consists of a driven element in the form of a spline-parameterized radiator fed through a microstrip line. The ground plane edge oriented toward the radiating component is also implemented in the form of a spline curve. The presented topology generates closely located resonant modes, which contribute to the broadband behavior [48,49]. Furthermore, the bandwidth-related performance is enhanced using an *L*-shaped ground plane stub, which improves the impedance matching of miniaturization-oriented designs [24]. The structure is implemented on a Rogers RO4003 dielectric substrate with a permittivity of 3.58, thickness of 0.813 mm, and loss tangent of 0.0027. The vector of the antenna input parameters is $\boldsymbol{y} = [\boldsymbol{y}_a\ \boldsymbol{y}_g\ \boldsymbol{y}_r]^T$, where $\boldsymbol{y}_a = [X\ l_f\ l_1\ l_{2r}\ w_1\ o_r]^T$, $\boldsymbol{y}_g = [y_{g.1}\ \ldots\ y_{g.L}]^T$ and $\boldsymbol{y}_r = [y_{r.1}\ \ldots\ y_{r.L}]^T$ ($L = 50$ represents the number of points used to represent the ground plane and radiator in the antenna model). The relative variables are $l_2 = (X - w_1)l_{2r}$, $Y = l_1 + w_1$, $l_{fr} = \min\{0.5X, 0.5(Y - l_f)\}$, $o = 0.5X + o_r$. Dimension $w_f = 1.8$ remains fixed to ensure 50 Ohm input impedance. The unit for all variables except dimensionless l_{2r} is mm. It should be noted that vectors $\boldsymbol{y}_g = Y{\cdot}\boldsymbol{z}_g$, and $\boldsymbol{y}_r = S{\cdot}\boldsymbol{z}_r$, where $S = \min\{0.5(X - o_r), 0.5(Y - l_f)\}$ represent the characteristic points (so-called knots) of the spline curves used to define the ground plane and radiator, respectively (see Figure 1). To ensure the structure consistency, the gap between each knot $\boldsymbol{y}_g$ and $\boldsymbol{y}_r$ is even. Hence, the vectors denote the relative distance of the curve from the reference point (edge of the substrate for $\boldsymbol{y}_g$ and center of the radiator for $\boldsymbol{y}_r$, respectively; Figure 1). It is worth emphasizing that $\boldsymbol{y}_r$ represents axial dimensions, as the parameters of the radiator are defined in a cylindrical coordinate system. The EM model of the antenna structure $\boldsymbol{R}$ is implemented in CST Microwave Studio and evaluated using its time domain solver.

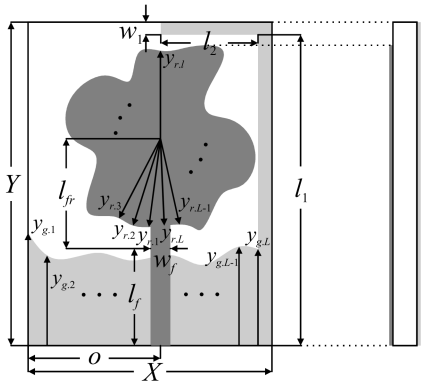

Figure 1. Geometry of the proposed spline-parameterized monopole antenna with highlights on its design parameters, showing top and cross-section views. The dark and light gray areas represent the radiator and ground-plane layers, respectively.

The presented antenna supports flexible parameterization. In other words, the number of adjustable variables used for representation of the structure geometry can be changed in the course of the design process. The rationale behind this feature is that—when the generation of compromise design solutions is considered—the initial search space ranges are set to be large to ensure that the optimal designs are captured within them. The application of conventional (population-based) methods for exploration of the search space with wide parameter ranges is numerically impractical due to the tremendous number of iterations required for convergence [38,43]. Having a model with adjustable dimensionality, one can narrow down the search space to the region of interest using a relatively small number of parameters. The promising region can be further exploited through optimizations of the model characterized by gradually increasing dimensionality. Flexible parameterization has been implemented through implicit handling of the input variables. Let $\boldsymbol{x}_d = [\boldsymbol{y}_a\ \boldsymbol{x}_{g.d}\ \boldsymbol{x}_{r.d}]^T$, where $\boldsymbol{x}_{g.d} = [x_{g.1}\ \ldots\ x_{g.d}]^T$, $\boldsymbol{x}_{r.d} = [x_{r.1}\ \ldots\ x_{r.d}]^T$, $d = 1, \ldots, L$ represent the d-knot spline curve used to represent the antenna ground plane and radiator, respectively. Note that when $d < 4$, $\boldsymbol{x}_{g.d} = x_{g.1}$ and $\boldsymbol{x}_{r.d} = x_{r.1}$, because the implementation of the spline used in this work requires at least four knots. The change of the antenna dimensionality is realized through the interpolation of $\boldsymbol{x}_{g.d}$ and $\boldsymbol{x}_{r.d}$ to $z_g = z_{g.L}$ and $z_r = z_{r.L}$ vectors, respectively. The process can be defined as follows:

$$\mathbf{z}_{\{g,r\}} \leftarrow sp\left(\mathbf{x}_{\{g,r\}.d}, L\right) \tag{1}$$

where sp is the function that realizes L-point spline-based interpolation of the d-dimensional input vector. The conversion process is transparent to the design optimization algorithm. The lower and upper bounds for the structure optimization are $\boldsymbol{l}_b = [6\ 4\ 10\ 0.05\ 0.5\ -1\ \boldsymbol{l}_{g.d}\ \boldsymbol{l}_{r.d}]^T$ and $\boldsymbol{u}_b = [30\ 15\ 30\ 1\ 2.5\ 1\ \boldsymbol{u}_{g.d}\ \boldsymbol{u}_{r.d}]^T$, where $\boldsymbol{l}_{g.d} = [0.2\ \ldots\ 0.2]^T$, $\boldsymbol{l}_{r.d} = [0.1\ \ldots\ 0.1]^T$, and $\boldsymbol{u}_{g.d} = [0.8\ \ldots\ 0.8]^T$, $\boldsymbol{l}_{r.d} = [1\ \ldots\ 1]^T$.

3. Design Methodology

In this section, the proposed design methodology is explained. To make the paper self-contained, a short discussion of the multi-objective design problem, followed by a brief description of the utilized optimization algorithm, are provided here. Next, the introduced multi-objective optimization method that permits a gradual increase of the number of antenna parameters is described. The section is concluded with the summary of the presented design framework. Numerical results are provided in Section 4.

3.1. Multi-Objective Design Problem

The multi-objective design problem can be defined as follows [39]:

$$\boldsymbol{x}^* \in \underset{\boldsymbol{x}\in\mathbf{X}}{\operatorname{argmin}} F(\boldsymbol{x}) \tag{2}$$

where $\boldsymbol{x} = \boldsymbol{x}_d$ (see Section 2) denotes the vector of the design parameters, $\boldsymbol{X}$ is the feasible region of the search space, and $\boldsymbol{x}^*$ represents the optimal design. The objective functions are given as

$$F(\boldsymbol{x}) = [F_1(\boldsymbol{x}), \ldots, F_q(\boldsymbol{x})]^T \tag{3}$$

where $q = 1, \ldots, Q$. Note that $F(\boldsymbol{x}) = F(\boldsymbol{R}(\boldsymbol{x}))$, where $\boldsymbol{R}(\boldsymbol{x})$ is a vector of responses obtained from EM evaluation of the antenna model at the design $\boldsymbol{x}$. The responses may represent the electrical performance (e.g., reflection over a frequency range or isolation between radiators), field (e.g., single-direction gain over the frequency or radiation pattern at the given frequency), or geometry (e.g., footprint or volume) of the structure. If $Q > 1$, the conventional notion of performance improvement known from single-objective optimization (i.e., the one based on direct comparison of the objective function responses obtained for candidate solutions) is not applicable [39]. Instead, designs can be compared using a domination relation [39]. One can say that the design $\boldsymbol{x}_1$ dominates over $\boldsymbol{x}_2$ if $F_q(\boldsymbol{x}_1) \leq F_q(\boldsymbol{x}_2)$ for all q and $F_q(\boldsymbol{x}_1) < F_q(\boldsymbol{x}_2)$ for at least one objective. A design $\boldsymbol{x}_q{}^*$ is optimal in the Pareto sense if there is no other design $\boldsymbol{x}_r{}^*$ ($q \neq r$), such that $\boldsymbol{x}_r{}^*$ dominates over $\boldsymbol{x}_q{}^*$. The solution to the multi-objective problem is a set of Pareto-optimal designs. For a more detailed description of the MO optimization concept, see [35,39,43].

3.2. Nested Optimization with a Variable Number of Design Parameters

Although conventional global-optimization algorithms proved to be useful for solving complex problems, they suffer from an unacceptable numerical cost, associated with the tremendous number of model evaluations required to find the optimal designs. On the other hand, deterministic algorithms (such as gradient or pattern search methods [36,50]) are often characterized by a lower computational cost yet limited capability in terms of escaping from local minima. In this work, the problem is mitigated by performing a series of optimizations in a nested loop. The latter gradually increases the number of design variables, first to identify and then to exploit the region of the search space of interest. The analogy to this approach, from the perspective of the design objective space, is observation of the landscape from a high altitude where the amount of visible details is limited. With each iteration of the nested loop (that is associated with an increasing the number of parameters), the "altitude" decreases, which allows the algorithm to "identify" more details of the landscape and improve the design response.

Let $\boldsymbol{d} = [d_1 \ldots d_n \ldots d_N]^T$, $d_n = 1, \ldots, L$, $n = 1, \ldots, N$ represent the set defining the number of spline parameters (positive integer values) used to represent the ground plane and radiator, respectively. In each step, the final d_n dimensional design $\boldsymbol{x}_{dn}{}^*$, obtained in the nth nested iteration, is used as a starting point for the $n + 1$ step. Assuming that the vector $\boldsymbol{d}$ is defined, n is set, and the initial design $\boldsymbol{x}_{dn}{}^*$ is available, the nested optimization can be summarized as follows:

1. Set $\boldsymbol{x}_{dn+1}{}^{(0)} \leftarrow sp(\boldsymbol{x}_{dn}{}^*, d_{n+1})$ (see Section 2);
2. Find design $\boldsymbol{x}_{dn+1}{}^*$ using $\boldsymbol{x}_{dn+1}{}^{(0)}$ as a starting point for optimization;
3. If $n = N$, END; otherwise, set $n = n + 1$ and go to 1.

It should be noted that the size N of vector $\boldsymbol{d}$ substantially affects the algorithm cost, as the optimization process is reset at each iteration $n = 1, \ldots, N$. On the other hand, the number of iterations and step size between d_n and d_{n+1} can be adjusted so as to mitigate the risk of getting stuck in a poor local optimum while managing the optimization cost at the acceptable level. Conceptual visualization of the objective function (a so-called feature) and design spaces for the structure, represented using the increasing number of parameters, is shown in Figure 2.

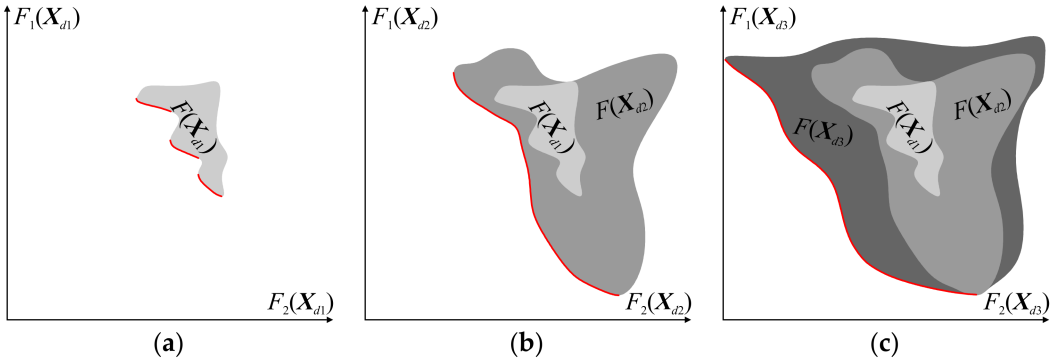

Figure 2. Conceptual illustration of the feature space for the bi-objective problem, characterized by a gradual increase of dimensionality. (**a**) d_1, (**b**) $d_2 > d_1$, and (**c**) $d_3 > d_2$. The red line represents the Pareto front [39]. Note that the solutions that are attainable for the structure represented using, for example, d_1 variables, represent a subset of the responses that can be found when the dimensionality is increased.

3.3. Generation of Trade-Off Designs

The presented bi-objective optimization algorithm involves two stages: (i) generation of the extreme (or corner) designs and (ii) sequential determination of the Pareto set using constrained optimizations. The first corner solution is obtained by solving the following minimization problem:

$$\boldsymbol{x}_{1.d_n}{}^{*} = \arg\min_{\boldsymbol{x}_{d_n} \in \mathbf{X}} F_1(\boldsymbol{x}_{d_n}) \tag{4}$$

Note that Equation (4) involves optimization of the structure in regard to a single objective. The second design is obtained through constrained optimization, oriented toward minimization of the second performance criterion:

$$\boldsymbol{x}_{2.d_n}{}^{*} = \arg \min_{\substack{\boldsymbol{x}_{d_n} \in \mathbf{X} \\ F_1(\boldsymbol{x}_{d_n}) \le F_{1.\max}}} F_2(\boldsymbol{x}_{d_n}) \tag{5}$$

The goal of Equation (5) is to minimize F_2 while ensuring that the response of the optimized design $\boldsymbol{x}_{2.dn}{}^{*}$ does not violate the defined threshold $F_{1.\max}$. The reasoning behind the introduction of a design constraint is to permit minimization of the second objective while maintaining the response regarding $F_1(\boldsymbol{x}_{dn})$ at an acceptable level. Generation of the extreme points is conceptually illustrated in Figure 3.

In the second stage, the algorithm sequentially identifies the Pareto designs. In each step, the new points are obtained between the already existing optimal solutions. Let $\boldsymbol{x}_{p.dn}{}^{*}$ ($p = 1, \ldots, l_k$; $l_k = 2^{k-1} + 1$) represent the Pareto designs obtained in the $k-1$ iteration, where $k = 1, \ldots, K$. It should be noted that $l_0 = 2$ refers to two corner designs—$\boldsymbol{x}_{1.dn}{}^{*}$, $\boldsymbol{x}_{2.dn}{}^{*}$—found in the first design stage. The candidate solutions are determined as follows:

$$\boldsymbol{x}_{c.d_m}^{(0)} = \left[\boldsymbol{x}^{*}{}_{p.d_m} + \boldsymbol{x}^{*}{}_{p+1.d_m}\right]/2 \tag{6}$$

where $c = l_k + b$ and $b = 1, \ldots, l_k - 1$. It should be noted that the reference designs in Equation (6) are approximated using d_m variables. Hence, the cth candidate design can be generated even when using $\boldsymbol{x}^{*}{}_{p.dn}$ and $\boldsymbol{x}^{*}{}_{p+1.do}$, $d_n \neq d_o$ ($o = 1, \ldots, N$). This is ensured by interpolating the reference designs' dimensionality as $\boldsymbol{x}_{p.dm}{}^{(0)} \leftarrow sp(\boldsymbol{x}_{p.dn}{}^{*}, d_m)$, $\boldsymbol{x}_{p+1.dm}{}^{(0)} \leftarrow sp(\boldsymbol{x}_{p+1.do}{}^{*}, d_m)$ (see Section 2). The obtained candidate solutions are utilized as starting points for constrained optimization:

$$\boldsymbol{x}_{c.d_n}{}^{*} = \arg \min_{\substack{\boldsymbol{x}_{c.d_n} \in \mathbf{X} \\ F_2(\boldsymbol{x}_{c.d_n}) \le F_{2.c.\max}}} F_1(\boldsymbol{x}_{c.d_n}) \tag{7}$$

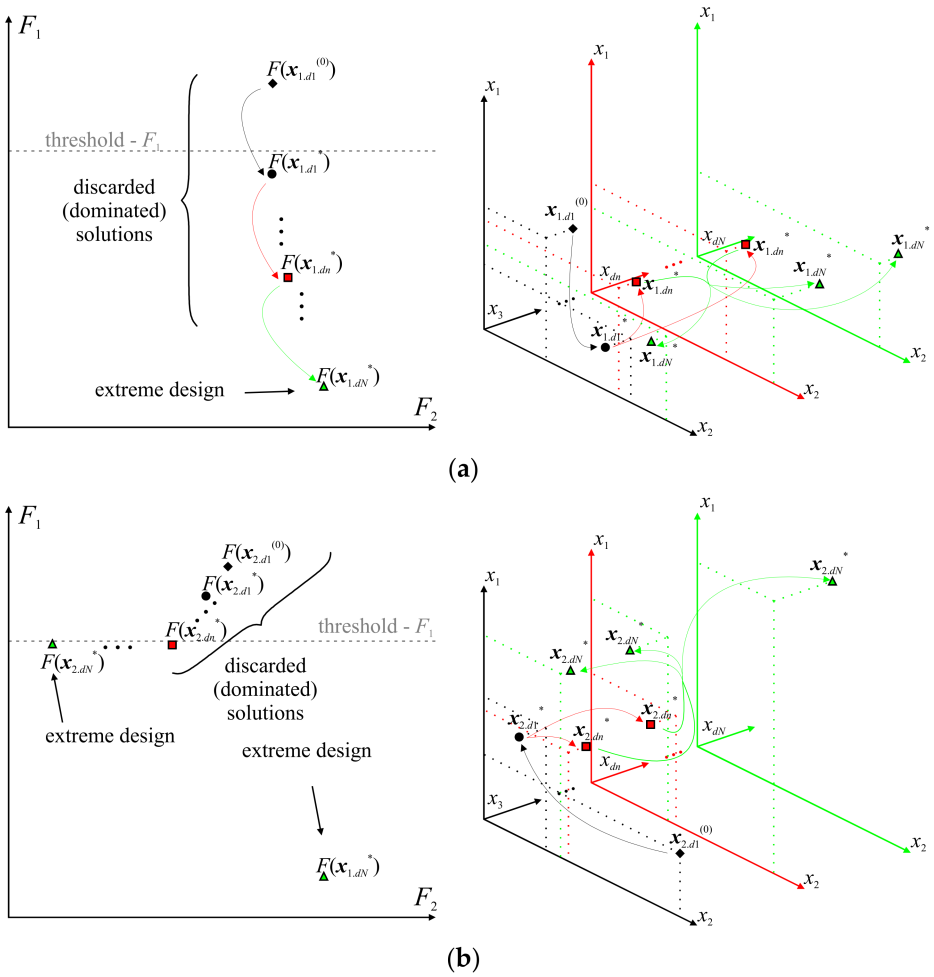

Figure 3. Generation of the extreme Pareto designs, with a conceptual illustration of the feature (**left**) and design (**right**) spaces; optimization w.r.t. (**a**) first and (**b**) second design objective. Note that the design space is represented in the form of three-dimensional projections (hence, the solutions for $d_1 = 3$ are shown only on the black plot, whereas the designs with d_n and d_N parameters are shown on two and three plots at a time). The optimal geometry obtained for the structure represented using d_{n-1} dimensional design is used as a starting point for optimization of the d_n dimensional antenna.

The goal of Equation (7) is to minimize the objective function F_1 while maintaining the structure response with respect to the second objective below the specified threshold. The latter is set to $F_{2.c.\max} = 0.5(F_2(\boldsymbol{x}_{p.dn}^{*}) + F_2(\boldsymbol{x}_{p+1.dn}^{*}))$. In order to facilitate generation of the Pareto set, the constraint on F_2 is implemented in the form of a penalty coefficient included with the objective function. The process in Equation (7) is performed in a nested optimization loop as shown in Section 3.2. As already mentioned, such an approach allows one to gradually increase the quality of the Pareto designs by appropriate adjustment of the antenna dimensionality. Finally, the designs $\{\boldsymbol{x}_{p.dn}^{*}\}_{p\,=\,1,\,\ldots\,,\,lk}$ and $\{\boldsymbol{x}_{c.dn}^{*}\}_{c\,=\,lk\,+\,(1,\,\ldots\,,\,lk-1)}$ are concatenated as $\{\boldsymbol{x}_{1.d}^{*}, \boldsymbol{x}_{b+1.dn}^{*}, \boldsymbol{x}_{2.dn}^{*}, \boldsymbol{x}_{b+2.dn}^{*}, \ldots, \boldsymbol{x}_{lk-1.dn}^{*}, \boldsymbol{x}_{2lk-1.dn}^{*}, \boldsymbol{x}_{lk.dn}^{*}\}$ and reindexed to $\{\boldsymbol{x}_{1.d}^{*}, \boldsymbol{x}_{2.dn}^{*}, \boldsymbol{x}_{3.dn}^{*}, \boldsymbol{x}_{4.dn}^{*}, \ldots, \boldsymbol{x}_{2lk-3.dn}^{*}, \boldsymbol{x}_{2lk-2.dn}^{*}, \boldsymbol{x}_{2lk-1.dn}^{*}\}$. The discussed optimization routine (see Figure 4 for a block diagram) can be summarized as follows:

1. Set the initial designs $\boldsymbol{x}_{1.d1}^{(0)}$ and $\boldsymbol{x}_{2.d1}^{(0)}$; set $\boldsymbol{d} = [d_1\ d_2\ \ldots\ d_m\ \ldots\ d_n\ \ldots\ d_N]^T$;
2. Obtain $\boldsymbol{x}_{1.dn}^{*}$ and $\boldsymbol{x}_{2.do}^{*}$ ($n \leq N$, $o \leq N$) by solving Equations (4) and (5) in a nested loop (see Section 3.2);
3. Set $k = 1$;
4. Set $p = 1$;
5. Set $\boldsymbol{x}_{p.dm}^{*} \leftarrow sp(\boldsymbol{x}_{p.dn}^{*}, d_m)$, $\boldsymbol{x}_{p+1.dm}^{*} \leftarrow sp(\boldsymbol{x}_{p+1.do}^{*}, d_m)$ (see Section 2), and then calculate $\boldsymbol{x}_{c.dm}^{(0)}$ and set $F_{2.c.\max}$;

6. Generate $\boldsymbol{x}_{c.dn}^{*}$ by solving Equation (7) in a nested optimization loop;
7. If $p = l_k$, go to 7; otherwise set $p = p + 1$ and go to 5;
8. Concatenate the designs as $\{\boldsymbol{x}_{1.d}^{*}, \boldsymbol{x}_{b+1.dn}^{*}, \boldsymbol{x}_{2.dn}^{*}, \boldsymbol{x}_{b+2.dn}^{*}, \ldots, \boldsymbol{x}_{lk-1.dn}^{*}, \boldsymbol{x}_{2lk-1.dn}^{*}, \boldsymbol{x}_{lk.dn}^{*}\}$, and then reindex the resulting set;
9. If $k = K$, END; otherwise, set $k = k + 1$ and go to 4.

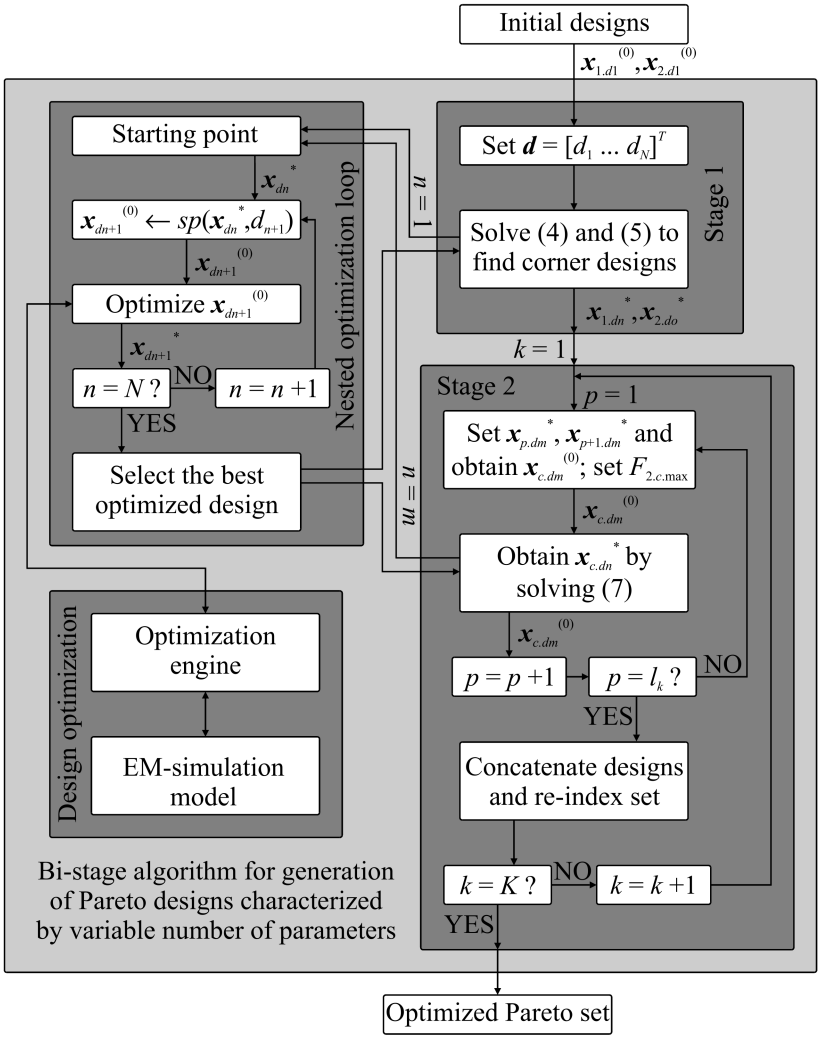

Figure 4. Block diagram of the proposed bi-objective optimization algorithm.

In the first stage of the presented framework, the initial designs $\boldsymbol{x}_{1.d1}^{(0)}$ and $\boldsymbol{x}_{2.d1}^{(0)}$ are obtained using a greedy search-based topology adjustment. The goal of the procedure is to find reasonable starting points for the optimization process. Upon identification of the initial designs, the generation of the Pareto set is handled by the above-outlined routine.

It is worth mentioning that the concept of generating intermediate designs is similar to the one presented in [47]. Here, however, the bisections are used only for the generation of candidate designs, which are further refined by means of constrained optimization. Furthermore, the algorithm of [47] does not support increasing the dimensionality of the problem in the course of structure optimization. Owing to the identification of new designs between the already existing ones, the algorithm allows for obtaining a Pareto set characterized by relatively even separation between the consecutive solutions (in the objective function space). Generation of the Pareto designs using the discussed algorithm is conceptually illustrated in Figure 5.

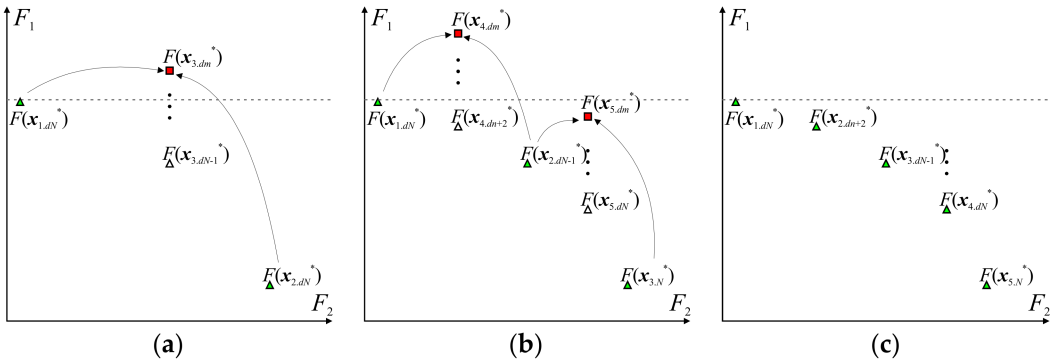

Figure 5. Generation of the optimal designs between the existing solutions for $K = 2$, where: (**a**) $k = 1$ (before reindexing), (**b**) $k = K$ (before reindexing), and (**c**) $k = K$ (after reindexing). Note that the candidate designs (red squares) are obtained through approximation of the geometries optimized in previous iterations using d_m dimensions. The white and green triangles represent the optimized designs before and after reindexing, respectively. The final designs can be represented using a varying number of variables.

3.4. Optimization Engine

The optimization engine used in this work for solving Equations (4), (5), and (7) is a local gradient method [36]. The algorithm is embedded in a trust region (TR) framework [37]. The latter generates a series ($i = 1, 2, 3, \ldots$) of local models around what is currently the best design $\boldsymbol{x}^{(i)}$ in order to gradually approximate the optimal solution to be found. The TR-based optimization is defined as [37]

$$\boldsymbol{x}^{(i+1)} = \arg \min_{\boldsymbol{x}:\|\boldsymbol{x}-\boldsymbol{x}^{(i)}\| \leq r^{(i)}} F\left(\boldsymbol{G}^{(i)}(\boldsymbol{x})\right) \tag{8}$$

where $\boldsymbol{G}^{(i)}$ is a first-order Taylor expansion model, given by [51]

$$\boldsymbol{G}^{(i)}(\boldsymbol{x}) = \boldsymbol{R}\left(\boldsymbol{x}^{(i)}\right) + \boldsymbol{J}\left(\boldsymbol{x}^{(i)}\right) \cdot \left(\boldsymbol{x} - \boldsymbol{x}^{(i)}\right) \tag{9}$$

where $\boldsymbol{J}(\boldsymbol{x}^{(i)})$ represents the Jacobian generated around $\boldsymbol{x}^{(i)}$ using a large-step finite differentiation [51]. The TR radius $r^{(i)}$ (i.e., the region around $\boldsymbol{x}^{(i)}$ for which the model is considered valid) is adjusted based on the calculated gain ratio [51]:

$$\rho = \frac{\boldsymbol{R}\left(\boldsymbol{x}^{(i+1)}\right) - \boldsymbol{R}\left(\boldsymbol{x}^{(i)}\right)}{\boldsymbol{G}^{(i)}\left(\boldsymbol{x}^{(i+1)}\right) - \boldsymbol{G}^{(i)}\left(\boldsymbol{x}^{(i+1)}\right)} \tag{10}$$

The candidate design $\boldsymbol{x}^{(i+1)}$ is accepted only if $\rho > 0$. Otherwise, the iteration is reset. The radius is updated according to the standard rules [37]. The initial value $r^{(0)}$ is controlled by the nested optimization loop (i.e., for $n = 1$, the radius is set to $r^{(0)} = 1$, whereas for $n > 1$, $r^{(0)} = 1/d_n$) (see Section 3.2). The algorithm is terminated either when the Euclidean distance between two consecutive designs or the radius are smaller than a specified threshold (i.e., $||\boldsymbol{x}^{(i+1)} - \boldsymbol{x}^{(i)}|| \leq \varepsilon$, or $r^{(i+1)} \leq \varepsilon$ (here, $\varepsilon = 10^{-2}$)). The algorithm can be summarized as follows:

1. Set $i = 0$ and $\boldsymbol{x}^{(0)}$, then set $r^{(0)}$ according to the iteration of the nested loop in Section 3.2;
2. Generate the Jacobian $\boldsymbol{J}(\boldsymbol{x}^{(i)})$ and construct the local approximation model $\boldsymbol{G}^{(i)}$;
3. Find $\boldsymbol{x}^{(i+1)}$ by solving Equation (8);
4. Evaluate $\boldsymbol{R}(\boldsymbol{x}^{(i+1)})$ and calculate ρ;
5. If $\rho > 0.75$, set $r^{(i+1)} = 2r^{(i)}$. If $\rho < 0.25$, set $r^{(i+1)} = r^{(i)}/3$;
6. If $\rho < 0$, go to 3; otherwise, go to 7;
7. If the termination condition is met, END; otherwise, set $i = i + 1$ and go to 2.

Owing to utilization of the Taylor model, the computational cost of the algorithm is low, as it requires $d_n + 1$ simulations of the $\boldsymbol{R}$ model per successful iteration. Additional evaluations are required for the steps that do not improve the objective function value. The justification for decreasing the initial radius when $n > 1$ is that with each iteration of the nested loop, the goal of the algorithm is to exploit the region identified in the previous step. For more comprehensive discussion on TR optimization methods, see [37,51].

4. Numerical Results

In this section, the presented antenna structure and design optimization algorithm are numerically validated. The design problem involves bi-objective optimization of the radiator for size reduction and minimization of reflection within the frequency band of interest. The obtained EM simulation results were verified based on evaluations performed using a frequency domain solver. Furthermore, the presented routine has been compared against a conventional multi-objective optimization algorithm in terms of computational cost and quality of the obtained Pareto designs. Finally, the smallest obtained antenna solution has been benchmarked against other structures from the literature. All computations have been performed using an Intel Xeon E5-2650 processor with 32 GB of RAM.

4.1. Bi-Objective Antenna Optimization

The design objectives for the considered antenna optimization problem included the following: the minimization of reflection F_1, such that $|S_{11}| = |\boldsymbol{R}(\boldsymbol{x})| = |\boldsymbol{R}(\boldsymbol{x}, f)|$, where $f = f_L, \ldots, f_H$ denotes the frequency points at which the radiator is evaluated (f_L = 3.1 GHz, f_H = 10.6 GHz), as well as the reduction of the structure footprint F_2, defined as $A(\boldsymbol{x}) = X \times Y$ rectangle (see Section 2).

The starting points for determination of the extreme Pareto designs were ${\boldsymbol{x}_{1.1}}^{(0)}$ = [10 6 16 0.8 1 0 0.35 0.6]^T and ${\boldsymbol{x}_{2.1}}^{(0)}$ = [24 10 27 0.2 1.5 0 0.4 0.8]^T. It is worth noting that, due to being represented using only one variable, the radiators and ground planes of the initial designs were in the forms of circles and rectangles, respectively. Both antenna geometries are shown in Figure 6. The objective function for optimization with respect to the first performance requirement was defined as

$$F_1(\boldsymbol{x}) = \alpha_1 E_1(\boldsymbol{x}) + \min\{0, E_2(\boldsymbol{x})\} \tag{11}$$

where

$$E_1(\boldsymbol{x}) = \frac{1}{M}\sum \left| \frac{|S_{11}|_{f_v} - S_{\max}}{S_{\max}} \right|^2 \tag{12}$$

$$E_2(\boldsymbol{x}) = \max(|S_{11}|) + S_{\max} \tag{13}$$

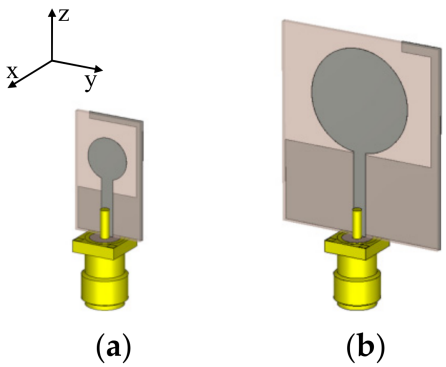

Figure 6. In-scale visualizations of the spline-parameterized antenna at the initial designs (**a**) ${\boldsymbol{x}_{1.1}}^{(0)}$ and (**b**) ${\boldsymbol{x}_{2.1}}^{(0)}$.

Here, $|S_{11}|_{fv}$ represents the reflection at M frequency points $f_v \in f$, the value of which was higher than the $S_{\max} = -15$ dB threshold. Note that the definition of Equation (12) in the least squares sense provided smooth changes of the objective function values in the course of the optimization process [51]. On the other hand, $E_1(\boldsymbol{x}) = 0$ when the antenna response was below $S_{\max}$ for all f_v points. In this case, the control over optimization was taken over by the min-max component in Equation (13). The scaling coefficient was set to $\alpha_1 = 10^4$ in order to ensure a smooth transition between the $E_1(\boldsymbol{x})$ and $E_2(\boldsymbol{x})$ functions. The second design objective was given as

$$F_2(\boldsymbol{x}) = \alpha_2 A(\boldsymbol{x})^2 + E_1(\boldsymbol{x}) \tag{14}$$

where $\alpha_2 = 0.01$ in order to ensure that the contribution of $E_1(\boldsymbol{x})$ to $F_2(\boldsymbol{x})$ was noticeable for a relatively small violation of $S_{\max} = F_{1.\max} = -11$ dB. It should be noted that for the majority of the antenna structures, a typical design requirement is to ensure that the reflection is below the -10 dB threshold. However, in practice, minimization of Equation (14) often leads to violation of the condition [43]. Setting a lower-than-required threshold $S_{\max}$ allowed us to ensure that $|S_{11}| \leq -10$ dB within the frequency band of interest.

The vector representing the dimensionality of the antenna (spline-based features of the structure) was $\boldsymbol{d} = [d_1 \ldots d_6]^T = [1\ 4\ 8\ 12\ 16\ 20]^T$. Hence, the number of nested optimizations per corner solution was $N = 6$. Moreover, $d_m = d_4 = 12$ (see Section 3.3). Figure 7 shows the antenna responses (corner points) obtained at each stage of the nested loop. The optimized corner designs were $\boldsymbol{x}_{1.d4}{}^* = \boldsymbol{x}_{1.12}{}^* = [26.07\ 10.56\ 28.56\ 0.06\ 0.5\ 0.51\ 0.38\ 0.44\ 0.46\ 0.41\ 0.47\ 0.39\ 0.36\ 0.44\ 0.43\ 0.42\ 0.43\ 0.59\ 0.78\ 0.77\ 0.71\ 0.73\ 0.81\ 0.75\ 0.65\ 0.72\ 0.9\ 0.88\ 0.78\ 0.75]^T$ and $\boldsymbol{x}_{2.d6}{}^* = \boldsymbol{x}_{2.20}{}^* = [12.54\ 4.16\ 16.22\ 0.66\ 2.14\ -0.19\ 0.35\ 0.37\ 0.33\ 0.27\ 0.22\ 0.2\ 0.2\ 0.2\ 0.2\ 0.23\ 0.4\ 0.37\ 0.34\ 0.35\ 0.34\ 0.34\ 0.32\ 0.32\ 0.31\ 0.23\ 0.46\ 0.5\ 0.53\ 0.52\ 0.48\ 0.44\ 0.45\ 0.5\ 0.55\ 0.61\ 0.7\ 0.73\ 0.66\ 0.62\ 0.65\ 0.64\ 0.69\ 0.74\ 0.73\ 0.64]^T$, respectively. Note that the dimensionality of the extreme points was different (12 relative variables per feature—30 total—for $\boldsymbol{x}_1{}^*$ vs. 20–46 total for $\boldsymbol{x}_2{}^*$), which was due to the lack of performance improvement from increasing the number of $\boldsymbol{x}_1$ variables above 12. The obtained solutions were used as starting points for generation of the Pareto set. In the second design stage, the Pareto designs were obtained using an objective of the following form:

$$F_{1.c}(\boldsymbol{x}) = F_1(\boldsymbol{x}) + (\max\{0, A(\boldsymbol{x}) - A_c\})^2 \tag{15}$$

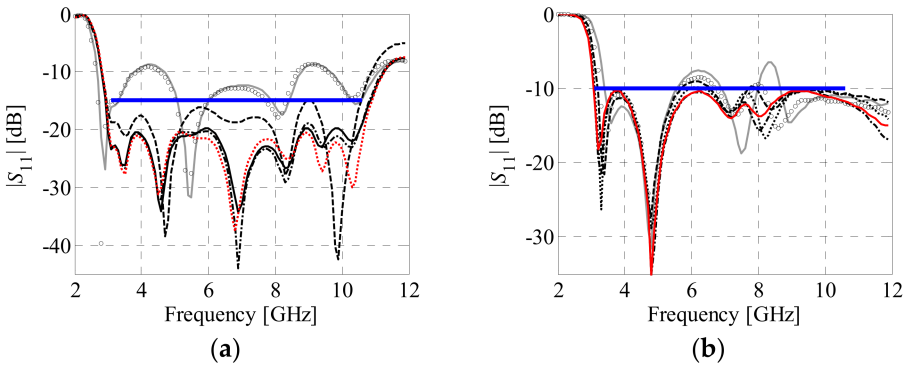

Figure 7. Reflection of the designs optimized in a nested loop with respect to (**a**) objective F_1 and (**b**) objective F_2. The dimensionalities of the spline-parameterized antenna features (see Section 2) are $d_1 = 1$ (gray), $d_2 = 4$ (○○○), $d_3 = 8$ (- -), $d_4 = 12$ (···), $d_5 = 16$ (·-·), and $d_6 = 20$ (—), respectively. The gray and red lines represent the characteristics of the initial and final designs obtained in the course of nested optimization. The blue lines denote the threshold values for the design objectives.

The additive component of Equation (15) is a penalty coefficient activated when the threshold $A_c = 0.5(A(\boldsymbol{x}_{m.d}{}^*) + A(\boldsymbol{x}_{m+1.d}{}^*))$ is violated. In $F_1(\boldsymbol{x})$, the parameter $S_{\max} = F_{1.c.\max}$ (see Section 3.3). The number of algorithm iterations was set to $K = 3$. The candidate

solutions for optimization were generated using Equation (6). The Pareto set, composed of two corner and seven intermediate designs {$\boldsymbol{x}_{1.20}{}^{*}$ $\boldsymbol{x}_{2.20}{}^{*}$ $\boldsymbol{x}_{3.20}{}^{*}$ $\boldsymbol{x}_{4.20}{}^{*}$ $\boldsymbol{x}_{5.20}{}^{*}$ $\boldsymbol{x}_{6.20}{}^{*}$ $\boldsymbol{x}_{7.20}{}^{*}$ $\boldsymbol{x}_{8.12}{}^{*}$ $\boldsymbol{x}_{9.12}{}^{*}$}, and the frequency responses of the selected optimal solutions are shown in Figure 8. The obtained results indicate that the footprints of the optimized antennas ranged from 230 mm^2 (with an in-band reflection of −10.3 dB) to 757 mm^2 (reflection of −20.5 dB). Hence, the change in antenna size and frequency responses along the Pareto set were 527 mm^2 and 10.2 dB, respectively. It is worth noting that the miniaturization rate of the smallest antenna with reference to the largest one was almost 70%. The gain pattern responses were obtained for the selected antenna designs (i.e., $\boldsymbol{x}_{1.20}{}^{*}$, $\boldsymbol{x}_{9.12}{}^{*}$ (corner designs), and $\boldsymbol{x}_{5.20}{}^{*}$ = [19.36 7.41 22.43 0.22 1.32 0.1 0.36 0.44 0.41 0.38 0.37 0.36 0.36 0.35 0.26 0.21 0.32 0.43 0.41 0.37 0.32 0.32 0.36 0.38 0.42 0.49 0.59 0.59 0.67 0.69 0.59 0.5 0.52 0.57 0.64 0.64 0.6 0.63 0.73 0.8 0.74 0.73 0.82 0.92 0.9 0.71]^T) (see Figure 9 for a visualization of the topologies). The characteristics shown in Figure 10 indicate that the $\boldsymbol{x}_{1.20}{}^{*}$ design was characterized by slightly more omnidirectional radiation patterns in the x–y plane and lower gain compared with the $\boldsymbol{x}_{5.20}{}^{*}$ and $\boldsymbol{x}_{9.12}{}^{*}$ geometries.

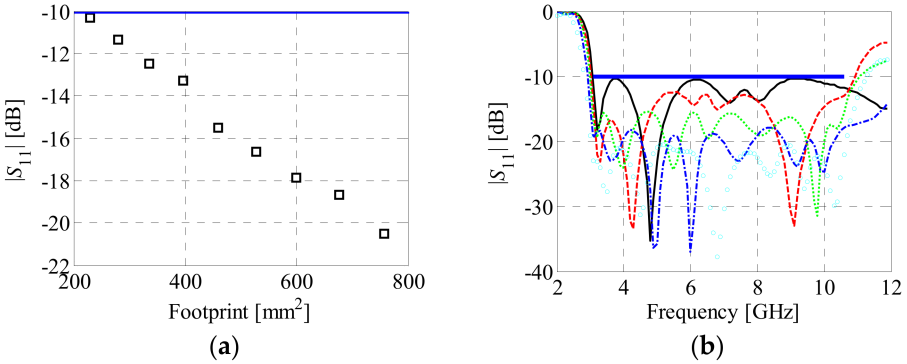

Figure 8. Spline-parameterized antenna's (**a**) Pareto set and (**b**) reflection responses obtained for the designs $\boldsymbol{x}_{1.20}{}^{*}$ (—), $\boldsymbol{x}_{3.20}{}^{*}$ (- -), $\boldsymbol{x}_{5.20}{}^{*}$ (···), $\boldsymbol{x}_{7.20}{}^{*}$ (·-·), and $\boldsymbol{x}_{9.12}{}^{*}$ (○○○).

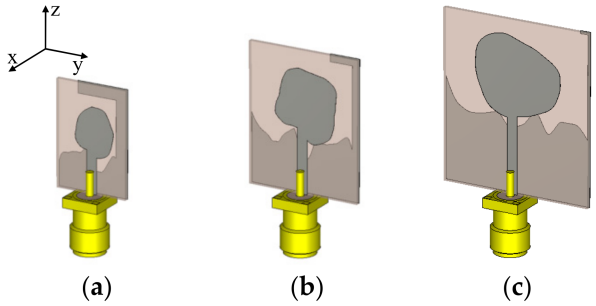

Figure 9. In-scale visualizations of the optimized antenna structures (**a**) $\boldsymbol{x}_{1.20}{}^{*}$, (**b**) $\boldsymbol{x}_{5.20}{}^{*}$, and (**c**) $\boldsymbol{x}_{9.12}{}^{*}$.

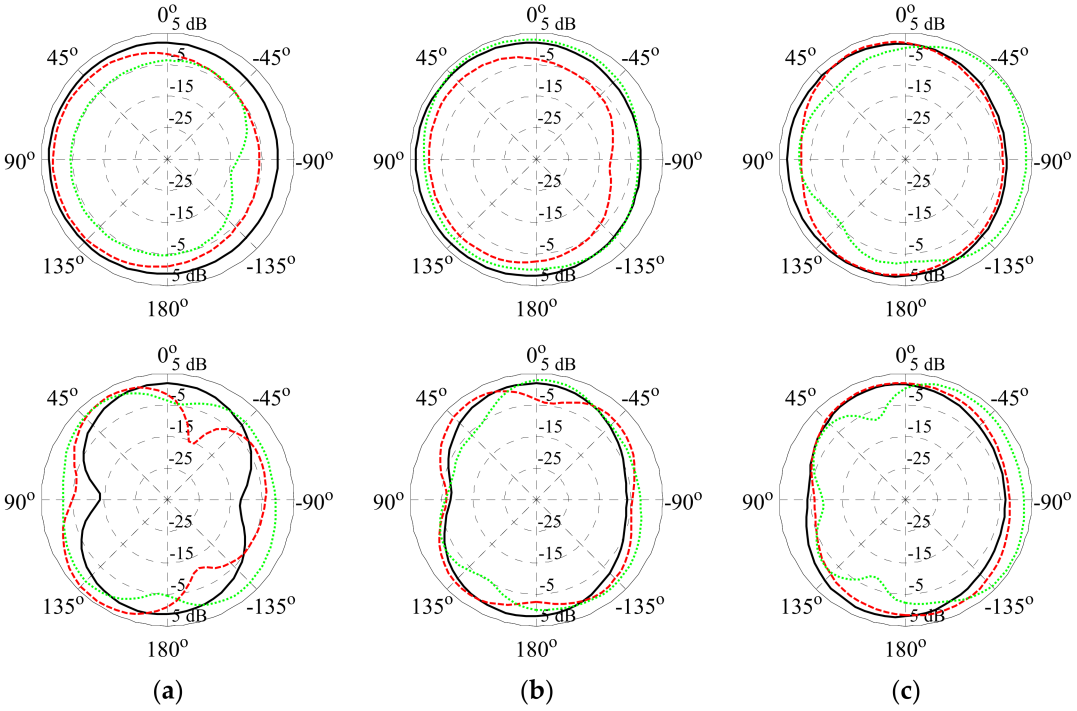

Figure 10. Realized gain patterns obtained at 4 GHz (–), 7 GHz (- -), and 10 GHz (···) for the optimized antenna designs (**a**) $\boldsymbol{x}_{1.20}^{*}$, (**b**) $\boldsymbol{x}_{5.20}^{*}$, and (**c**) $\boldsymbol{x}_{9.12}^{*}$. The top and bottom plots represent the characteristics obtained in the x–y and x–z planes (see Figure 9), respectively.

4.2. Comparisons and Discussion

To confirm the validity of the numerical results, the $\boldsymbol{x}_{1.20}^{*}$, $\boldsymbol{x}_{5.20}^{*}$, and $\boldsymbol{x}_{9.12}^{*}$ designs were evaluated using a frequency domain solver (finite elements method with adaptive meshing) implemented in CST Studio [52]. The response characteristics (shown in Figure 11) obtained using the time and frequency domain methods were similar, which indicates that the EM models used in the optimization process were valid. Furthermore, the plots of Figure 11 show that, at the lower corner frequency of 3.1 GHz, the $\boldsymbol{x}_{1.20}^{*}$, $\boldsymbol{x}_{5.20}^{*}$, and $\boldsymbol{x}_{9.12}^{*}$ designs featured radiation efficiencies of 76%, 89%, and 99%, respectively. Note that for the $\boldsymbol{x}_{1.20}^{*}$ design, an efficiency of over 90% was achieved above the 3.4 GHz frequency, which is considered acceptable, keeping in mind its small footprint. Overall, the considered antennas were characterized by average in-band efficiencies of 93%, 97%, and 98%, respectively. Clearly, the high values were due to the utilization of a low-loss substrate for implementation of the structures.

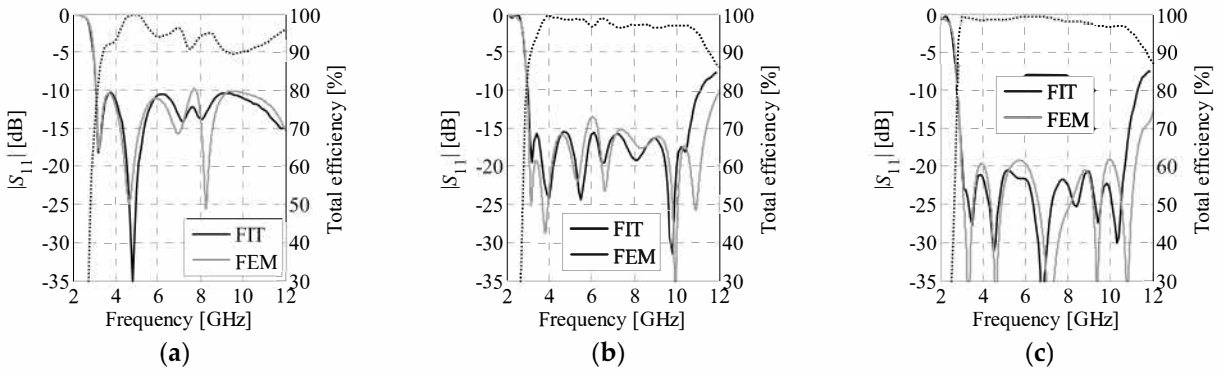

Figure 11. Comparison of EM simulation results obtained using solvers based on the finite integration technique (FIT) and finite elements method (FEM) for the designs (**a**) $\boldsymbol{x}_{1.20}^{*}$, (**b**) $\boldsymbol{x}_{5.20}^{*}$, and (**c**) $\boldsymbol{x}_{9.12}^{*}$. The dotted lines represent the total efficiency, evaluated using the FIT method.

Figure 12a shows a comparison of the optimal solutions obtained at different iterations of the nested loop (represented using a varying number of parameters). As can be seen, for the majority of the designs, increasing the dimensionality resulted in improvement in the structure responses. However, for certain solutions, a larger number of variables led to performance degradation. This was due to insufficient precision of the spline approximation when the number of knots increased, which led to undesirable frequency shifts at the edges of the operational bandwidth. Notwithstanding this, for most of the designs, the imperfections were corrected by the optimization algorithm.

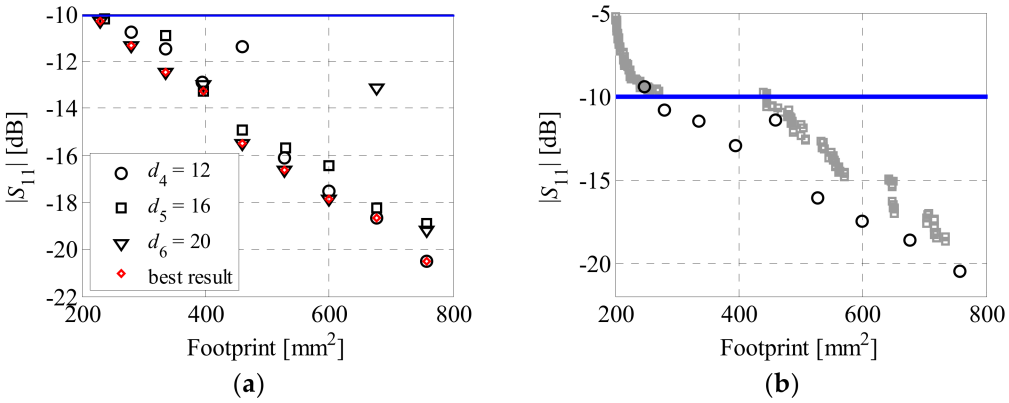

Figure 12. Comparison of the optimized antenna designs obtained using (**a**) different numbers of adjustable parameters, as well as (**b**) conventional MOEA and the presented nested algorithm (d_4 = 12).

The computational cost of bi-objective optimization corresponded to 4389 evaluations of the EM antenna model (~159.7 h of CPU time). The cost breakdown, with emphasis on individual nested loops, is gathered in Table 1. It should be noted that the average numerical expenses associated with the identification of a single Pareto-optimal design corresponded to about 488 ***R*** model evaluations, which is low when having in mind the dimensionality of the problem (up to 46 independent parameters). It is also worth noting that optimization of the designs represented using more than 30 variables amounted to 57% of the overall cost. For the sake of comparison, the antenna at hand was also optimized using a standard population-based multi-objective evolutionary algorithm (MOEA) with fitness sharing, mating restrictions, and Pareto dominance tournament selection [53]. The setup of the benchmark routine was as follows. The population size and the number of generations were set to 200 and 50 (a total of 10,000 EM simulations), respectively, whereas the probability of mutation and crossover were fixed at 0.2 and 0.5, respectively. Since the discussed algorithm did not support adjusting the antenna dimensionality, the number of parameters was set to 30 (i.e., d_4 = 12). Furthermore, the corner designs obtained using the method in Section 3 were included into the initial population. The latter was generated between the extreme points in order to narrow down the search space to the region of interest. Figure 12b shows a comparison of the designs obtained using both routines (the plots present the responses obtained for the antenna model, represented using 30 parameters). As can be seen, the algorithm of Section 3 outperformed the benchmark method in terms of performance of the resulting designs. More importantly, the number of ***R*** simulations required to obtain the final designs using the proposed algorithm amounted to 1889, which was 81% less compared to the cost of MOEA operation. Even when the optimization was performed in a nested loop, the cost of the presented algorithm (4389 EM simulations) was over two times lower compared with the benchmark routine (while providing noticeably better responses characterized by a more even spread between the extreme designs and better in-band reflection).

Table 1. Cost breakdown of the multi-objective optimization of the spline-parameterized antenna.

Design	Number of Model Evaluations [R]						Total [R]	Total [h]
	n = 1	n = 2	n = 3	n = 4	n = 5	n = 6		
$x_{1 \cdot dn}^{*}$	64	92	94	156	326	284	1016	36.97
$x_{2 \cdot dn}^{*}$	N/A	N/A	N/A	187	2	192	381	13.86
$x_{3 \cdot dn}^{*}$	N/A	N/A	N/A	158	41	145	344	12.52
$x_{4 \cdot dn}^{*}$	N/A	N/A	N/A	193	119	98	410	14.92
$x_{5 \cdot dn}^{*}$	N/A	N/A	N/A	128	198	146	472	17.18
$x_{6 \cdot dn}^{*}$	N/A	N/A	N/A	127	119	284	530	19.28
$x_{7 \cdot dn}^{*}$	N/A	N/A	N/A	158	41	238	437	15.90
$x_{8 \cdot dn}^{*}$	N/A	N/A	N/A	156	81	96	333	12.12
$x_{9 \cdot dn}^{*}$	56	46	118	156	40	50	466	16.96
Total	120	138	212	1419	967	1533	4389	159.71

One should emphasize that the dimensions of the smallest Pareto-optimal antenna design were only 12.5 mm × 18.4 mm (footprint = 230.4 mm^2). The structure was compared against other compact UWB monopoles from the literature in terms of size and bandwidth. For the sake of fair comparison, the dimensions of the considered structures were expressed in terms of the guided wavelength λ_g calculated for the lower corner frequency and the electrical performance of the substrates on which the considered radiators were implemented. The results gathered in Table 2 indicate that the proposed structure was characterized by a competitive size while providing acceptable performance. Small dimensions make the design's potential use not only for a range of mobile UWB sensors and IoT-based localization services, but also for body of area network applications [54].

Table 2. Spline-parameterized antenna ($x_{1.20}^{*}$) in comparison with the benchmark designs.

Antenna	f_L [GHz]	Bandwidth [GHz]	Dimensions [mm × mm]	Size [mm^2]	Dimensions [$\lambda_g \times \lambda_g$]	Footprint # [λ_g^2]
[55]	2.9	6.6	32.0 × 36.0	1152	0.56 × 0.64	0.359
[56]	3.0	8.0	28.0 × 38.0	1064	0.51 × 0.69	0.352
[57]	3.1	8.4	14.5 × 28.0	406	0.27 × 0.52	0.140
[11]	2.9	19.3	25.0 × 17.0	425	0.44 × 0.30	0.132
[18]	3.0	7.8	10.0 × 32.5	325	0.18 × 0.59	0.106
[54]	3.0	7.6	10.0 × 25.0	250	0.17 × 0.43	0.073
[58]	3.1	8.3	7.00 × 25.0	175	0.13 × 0.47	0.061
This work	3.1	8.9	12.5 × 18.4	230	0.32 × 0.22	0.069

For fair comparison, the antenna size is expressed in terms of the guided wavelength corresponding to the substrate properties the design is implemented on.

5. Conclusions

In this work, a spline-based UWB monopole antenna with an adjustable number of parameters has been presented. The structure has been optimized in a bi-objective setup using an algorithm that enables sequential generation of the Pareto designs between the extreme solutions. Each step of the design process involves a trust region-based optimization of the structure in a nested loop. The latter gradually increases the dimensionality of the antenna. The trade-off solutions are generated through the optimization of candidate designs, determined from bisections between the already existing solutions. The proposed method was used to obtain a total of nine antenna designs, representing compromises between a minimization of reflection within 3.1 GHz to 10.6 GHz band and size reduction. The geometries of the optimized radiators were represented using 30 to 46 independent parameters. The performance and sizes of the final designs along the Pareto front varied from −10.3 dB to −20.5 dB and from 230 mm^2 to 757 mm^2, respectively. The method has been favorably validated against a genuine multi-objective optimization algorithm in terms of computational cost and the quality of the obtained solutions. Furthermore, the smallest

Pareto-optimal antenna was compared against the state-of-the-art monopoles from the literature. The optimized radiator is characterized not only by competitive performance, but also a small footprint, which makes it of potential use for UWB sensors, mobile localization services, or body area networks. It is worth noting that the availability of the Pareto set provides the designer a detailed insight into the capabilities of the antenna for a range of application scenarios, which might be of high importance when designing heterogeneous sensors or IoT networks dedicated to operating in diverse environments is considered.

Future work will focus on the application of spline-parameterized antenna models to problems defined using more complex sets of requirements. The development of routines oriented toward reduction of the optimization cost will also be considered.

Author Contributions: A.B. and S.K. realized the conceptual work, and A.B. developed the design method, implemented the framework, and performed numerical experiments. K.Z. and P.P. performed part of the data analysis. All the authors were involved in the preparation of the manuscript. All authors have read and agreed to the published version of the manuscript.

Funding: This work was supported in part by the National Science Centre of Poland Grant 2017/27/B/ST7/00563 and by the National Centre for Research and Development Grant NOR/ POLNOR/HAPADS/0049/2019-00.

Informed Consent Statement: Not applicable.

Data Availability Statement: Not applicable.

Conflicts of Interest: The authors declare no conflict of interest.

References

1. Costanzo, A.; Dardari, D.; Aleksandravicius, J.; Decarli, N.; Del Prete, M.; Fabbri, D.; Fantuzzi, M.; Guerra, A.; Masotti, D.; Pizzotti, M.; et al. Energy autonomous UWB localization. *IEEE J. Radio Freq. Identif.* **2017**, *1*, 228–244. [CrossRef]
2. Cruz, C.C.; Costa, J.R.; Fernandes, C.A. Hybrid UHF/UWB antenna for passive indoor identification and localization systems. *IEEE Trans. Antennas Prop.* **2013**, *61*, 354–361. [CrossRef]
3. Li, M.G.; Zhu, H.; You, S.Z.; Tang, C.Q. UWB-based localization system aided with inertial sensor for underground coal mine applications. *IEEE Sens. J.* **2020**, *20*, 6652–6669. [CrossRef]
4. Decarli, N.; Guidi, F.; Dardari, D. Passive UWB RFID for tag localization: Architectures and design. *IEEE Sens. J.* **2016**, *16*, 1385–1397. [CrossRef]
5. Beuchat, P.N.; Hesse, H.; Domahidi, A.; Lygeros, J. Enabling optimization-based localization for IoT devices. *IEEE IoT J.* **2019**, *6*, 5639–5650. [CrossRef]
6. Xu, Y.; Shmaliy, Y.S.; Li, Y.; Chen, X. UWB-based indoor human localization with time-delayed data using EFIR filtering. *IEEE Access* **2017**, *5*, 16676–16683. [CrossRef]
7. Ko, H.; Pack, S. OB-DETA: Observation-based directional energy transmission algorithm in energy harvesting networks. *J. Comm. Netw.* **2019**, *21*, 168–176. [CrossRef]
8. Kim, J.H.; Cho, S.I.; Kim, H.J.; Choi, J.W.; Jang, J.E.; Choi, J.P. Exploiting the mutual coupling effect on dipole antennas for RF energy harvesting. *IEEE Antennas Wirel. Prop. Lett.* **2016**, *15*, 1301–1304. [CrossRef]
9. Shen, S.; Chiu, S.; Murch, R.D. A dual-port triple-band L-probe microstrip patch rectenna for ambient RF energy harvesting. *IEEE Antennas Wirel. Prop. Lett.* **2017**, *16*, 3071–3074. [CrossRef]
10. Liu, S.; Yang, D.; Chen, Y.; Huang, S.; Xiang, Y. Broadband Dual Circularly Polarized Dielectric Resonator Antenna for Ambient Electromagnetic Energy Harvesting. *IEEE Trans. Antennas Propag.* **2020**, *68*, 4961–4966. [CrossRef]
11. Tiwari, R.N.; Singh, P.; Kanaujia, B.K. A modified microstrip line fed compact UWB antenna for WiMAX/ISM/WLAN and wireless communications. *AEU Int. J. Electron. Commun.* **2019**, *104*, 58–65. [CrossRef]
12. Liu, J.-L.; Su, T.; Liu, Z.-X. High-Gain Grating Antenna With Surface Wave Launcher Array. *IEEE Antennas Wirel. Propag. Lett.* **2018**, *17*, 706–709. [CrossRef]
13. Hotte, D.; Siragusa, R.; Duroc, Y.; Tedjini, S. A concept of pressure sensor based on slotted waveguide antenna array for passive MMID sensor networks. *IEEE Sens. J.* **2016**, *16*, 5583–5587. [CrossRef]
14. Song, R.; Chen, X.; Jiang, S.; Hu, Z.; Liu, T.; Calatayud, D.G.; Mao, B.; He, D. A graphene-assembled film based MIMO antenna array with high isolation for 5G wireless communication. *Appl. Sci.* **2021**, *11*, 2382. [CrossRef]
15. Kwon, O.H.; Park, W.B.; Yun, J.; Lim, H.J.; Hwang, K.C. A low-profile HF meandered dipole antenna with a ferrite-loaded artificial magnetic conductor. *App. Sci.* **2021**, *11*, 2237. [CrossRef]
16. Khan, M.S.; Capobianco, A.D.; Asif, S.M.; Anagnostou, D.E.; Shubair, R.M.; Braaten, B.D. A compact CSRR-enabled UWB diversity antenna. *IEEE Antennas Wirel. Propag. Lett.* **2017**, *16*, 808–812. [CrossRef]

17. Alsath, M.G.N.; Kanagasabai, M. Compact UWB Monopole Antenna for Automotive Communications. *IEEE Trans. Antennas Propag. Lett.* **2015**, *63*, 4204–4208. [CrossRef]
18. Liu, Y.; Wang, P.; Qin, H. Compact ACS-fed UWB monopole antenna with extra Bluetooth band. *Electron. Lett.* **2014**, *50*, 1263–1264. [CrossRef]
19. Dumoulin, A.; John, M.; Ammann, M.J.; McEvoy, P. Optimized monopole and dipole antennas for UWB asset tag location systems. *IEEE Trans. Antennas Propag. Lett.* **2012**, *60*, 2896–2904. [CrossRef]
20. Nair, S.M.; Shameena, V.A.; Dinesh, R.; Mohanan, P. Compact semicircular directive dipole antenna for UWB applications. *Electron. Lett.* **2011**, *47*, 1260–1262. [CrossRef]
21. Yeoh, W.S.; Rowe, W.S.T. An UWB Conical Monopole Antenna for Multiservice Wireless Applications. *IEEE Antennas Wirel. Propag. Lett.* **2015**, *14*, 1085–1088. [CrossRef]
22. Yang, J.; Kishk, A. A novel low-profile compact directional ultra-wideband antenna: The self-grounded bow-tie antenna. *IEEE Trans. Antennas Propag. Lett.* **2012**, *60*, 1214–1220. [CrossRef]
23. Chu, Q.X.; Mao, C.X.; Zhu, H. A compact notched band UWB slot antenna with sharp selectivity and controllable bandwidth. *IEEE Trans. Antennas Propag. Lett.* **2013**, *61*, 3961–3966. [CrossRef]
24. Liu, L.; Cheung, S.W.; Yuk, T.I. Compact MIMO Antenna for Portable Devices in UWB Applications. *IEEE Trans. Antennas Propag. Lett.* **2013**, *61*, 4257–4264. [CrossRef]
25. Roshna, T.K.; Deepak, U.; Sajitha, V.R.; Vasudevan, K.; Mohanan, P. A compact UWB MIMO antenna with reflector to enhance isolation. *IEEE Trans. Antennas Propag. Lett.* **2015**, *63*, 1873–1877. [CrossRef]
26. Karimipour, M.; Aryanian, I. Demonstration of Broadband Reflectarray Using Unit Cells With Spline-Shaped Geometry. *IEEE Trans. Antennas Propag. Lett.* **2019**, *67*, 3831–3838. [CrossRef]
27. Dong, B.; Yang, J.; Dahlström, J.; Flygare, J.; Pantaleev, M.; Billade, B. Optimization and realization of quadruple-ridge flared horn with new spline-defined profiles as a high-efficiency feed from 4.6 GHz to 24 GHz. *IEEE Trans. Antennas Propag. Lett.* **2019**, *67*, 585–590. [CrossRef]
28. Ghassemi, M.; Bakr, M.; Sangary, N. Antenna design exploiting adjoint sensitivity-based geometry evolution. *IET Microw. Antennas Propag.* **2013**, *7*, 268–276. [CrossRef]
29. Lizzi, L.; Viani, F.; Azaro, R.; Massa, A. Optimization of a spline-shaped UWB antenna by PSO. *IEEE Antennas Wirel. Propag. Lett.* **2007**, *6*, 182–185. [CrossRef]
30. Toivanen, J.I.; Mäkinen, R.A.; Rahola, J.; Järvenpää, S.; Ylä-Oijala, P. Gradient-based shape optimisation of ultra-wideband antennas parameterised using splines. *IET Microw. Antennas Propag.* **2010**, *4*, 1406–1414. [CrossRef]
31. Ding, M.; Jin, R.; Geng, J.; Wu, Q.; Yang, G. Auto-design of band-notched UWB antennas using mixed model of 2D GA and FDTD. *Electron. Lett.* **2008**, *44*, 257–258. [CrossRef]
32. Mirhadi, S.; Komjani, N.; Soleimani, M. Ultra wideband antenna design using discrete Green's functions in conjunction with binary particle swarm optimization. *IET Microw. Antennas Propag.* **2016**, *10*, 184–192. [CrossRef]
33. Chandra, A.P.T.S.; Senthilkumar, L.; Meenakshi, M. Material distributive topology design of UWB antenna using parallel computation of improved BPSO with FDTD. *Int. J. Microw. Wirel. Technol.* **2018**, *11*, 190–198. [CrossRef]
34. Lalbakhsh, A.; Afzal, M.U.; Esselle, K.P.; Smith, S. Design of an artificial magnetic conductor surface using an evolutionary algorithm. In Proceedings of the International Conference on Electromagnetics in Advanced Applications (ICEAA), Verona, Italy, 11–15 September 2017; pp. 885–887.
35. Coello, C.A.C.; Van Veldhuizen, D.A.; Lamont, G.B. *Evolutionary Algorithms for Solving Multi-Objective Problems*, 2nd ed.; Springer: New York, NY, USA, 2007.
36. Nocedal, J.; Wright, S. *Numerical Optimization*, 2nd ed.; Springer: New York, NY, USA, 2006.
37. Gould, N.I.; Leyffer, S.; Toint, P.L. *Trust-Region Methods*; MPS-SIAM Series on Optimization; SIAM: Philadelphia, PA, USA, 2000.
38. Chen, Y.S.; Chiu, Y.H. Application of multiobjective topology optimization to miniature ultrawideband antennas with enhanced pulse preservation. *IEEE Antennas Wirel. Propag. Lett.* **2016**, *15*, 842–845. [CrossRef]
39. Deb, K. *Multi-Objective Optimization Using Evolutionary Algorithms*; Wiley: New York, NY, USA, 2001.
40. Tung, L.V.; Manh, L.H.; Ngoc, C.D.; Beccaria, M.; Pirinoli, P. Automated design of microstrip patch antenna using ant colony optimization. In Proceedings of the International Conference on Electromagnetics in Advanced Applications, Granada, Spain, 9–13 September 2019; pp. 0587–0590.
41. Lalbakhsh, A.; Afzal, M.U.; Zeb, B.A.; Esselle, K.P. Design of a dielectric phase-correcting structure for an EBG resonator antenna using particle swarm optimization. In Proceedings of the 2015 International Symposium on Antennas and Propagation, Hobart, Tasmania, Australia, 9–12 November 2015; pp. 1–3.
42. Lalbakhsh, A.; Esselle, K.P.; Smith, S.L. Design of a single-slab low-profile frequency selective surface. In Proceedings of the Progress in Electromagnetics Research Symposium, Singapore, 22–25 May 2017.
43. Koziel, S.; Bekasiewicz, A. *Multi-Objective Design of Antennas Using Surrogate Models*; World Scientific: Singapore, 2016.
44. Jin, N.; Rahmat-Samii, Y. Advances in particle swarm optimization for antenna designs: Real-number, binary, single-objective and multiobjective implementations. *IEEE Trans. Antennas Propag. Lett.* **2007**, *55*, 556–567. [CrossRef]
45. Mroczka, J. The cognitive process in metrology. *Measurement* **2013**, *46*, 2896–2907. [CrossRef]
46. Simpson, T.W.; Poplinski, J.D.; Koch, P.N.; Allen, J.K. Metamodels for computer-based engineering design: Survey and recommendations. *Eng. Comput.* **2001**, *17*, 129–150. [CrossRef]

47. Koziel, S.; Bekasiewicz, A. Pareto ranking bisection algorithm for expedited multi-objective optimization of antenna structures. *IEEE Antennas Wirel. Propag. Lett.* **2017**, *16*, 1488–1491. [CrossRef]
48. Valderas, D.; Sancho, J.I.; Puente, D.; Ling, C.; Chen, X. *Ultrawideband Antennas: Design and Applications*; Imperial College Press: London, UK, 2011.
49. Liang, J.; Chiau, C.C.; Chen, X.; Parini, C.G. Study of a printed circular disc monopole antenna for UWB systems. *IEEE Trans. Antennas Propag. Lett.* **2005**, *53*, 3500–3504. [CrossRef]
50. Kolda, T.G.; Lewis, R.M.; Torczon, V. Optimization by direct search: New perspectives on some classical and modern methods. *SIAM Rev.* **2003**, *45*, 385–482. [CrossRef]
51. Bekasiewicz, A. Low-cost automated design of compact branch-line couplers. *Sensors* **2020**, *20*, 3562. [CrossRef] [PubMed]
52. *CST Microwave Studio*; version 2015; Dassault Systems: Vélizy-Villacoublay, France, 2015.
53. Fonseca, C.M. Multiobjective Genetic Algorithms with Application to Control Engineering Problems. Ph.D. Thesis, Department of Automatic Control and Systems Engineering, University of Sheffield, Sheffield, UK, 1995.
54. Chahat, N.; Zhadobov, M.; Sauleau, R.; Ito, K. A compact UWB antenna for on-body applications. *IEEE Trans. Antennas Propag. Lett.* **2011**, *59*, 1123–1131. [CrossRef]
55. Gupta, M.; Mathur, V. Wheel shaped modified fractal antenna realization for wireless communications. *AEU Int. J. Electron. Commun.* **2017**, *79*, 257–266. [CrossRef]
56. Gopikrishna, M.; Krishna, D.D.; Aanandan, C.K.; Mohanan, P.; Vasudevan, K. Design of a microstip fed step slot antenna for UWB communication. *Microw. Opt. Technol. Lett.* **2009**, *51*, 1126–1129. [CrossRef]
57. Chung, W.T.; Lee, C.H. Compact Slot Antenna for UWB Applications. *IEEE Antennas Wirel. Propag. Lett.* **2010**, *9*, 63–66.
58. Roshna, T.K.; Deepak, U.; Sajitha, V.R.; Mohanan, P. Coplanar stripline-fed compact UWB antenna. *Electron. Lett.* **2014**, *50*, 1181–1182. [CrossRef]